



PROPOSITION OF A SPECTRAL AMPLIFICATION MODEL FOR NEAR FAULT DIRECTIVITY EFFECT WITH UTILIZING PROBABILISTIC EARTHQUAKE SCENARIOS

Saed MOGHIMI^{1,*}, Sinan AKKAR²

¹ Civil Engineering Department, Engineering Faculty, İstanbul Aydın University, İstanbul, Turkey

² Earthquake Engineering Department, Kandilli Observatory and Earthquake Research Institute,
Boğaziçi University, İstanbul, Turkey

ABSTRACT

Near fault ground motions with directivity effect show larger spectral demands due to their specific waveform features. Directivity effect occur due to S-wave polarization when the fault rupture propagation and waveform travel direction coincide on each other. In this situation, a pulse arises in the beginning of ground motion displacement and velocity waveforms which is mostly seen in the fault normal direction. The pulse period (T_p) is directly proportional to the earthquake magnitude (moment magnitude, M_w) and its amplitude is inversely proportional to the rupture distance (R_{rup}) from the site. The other characteristic of the near fault ground motions due to S-wave polarization is known as "Fling Step" in which a residual displacement is seen in the fault parallel displacement waveform. This study summarizes the observations from the effect of near fault ground motions on design spectrum. The results of these observations are used to develop simplified equations for incorporation of near fault effect in design spectrum. Probabilistic seismic hazard scenarios are utilized in this study in order to investigate the effect of fault seismicity, fault length (characteristic magnitude of the fault), pulse period and source-to-site geometry on the level of spectral amplification due to directivity effect. The near fault effect is modelled with assembling two narrow-band directivity models (Shahi and Baker 2011; Chiou and Spudich 2013) on the probabilistic seismic hazard scenarios respectively. In the last part of this study the significance of seismological and geometrical parameters on the level of spectral amplification due to directivity will be shown and discussed. The results are used to propose relationships for the incorporation of near fault directivity effect for different geometrical distributions of the sites around the fault.

Keywords: Directionality effect, Near fault ground motions, Earthquake hazard, Earthquake design codes

1. INTRODUCTION

One of the most important features of near fault ground motions with directivity effect is the impulsive signals which is mostly seen in the beginning of their velocity waveforms. Directivity effect is verified in several near fault ground motions during last decades (e.g., Port Hueneme earthquake in 1957 [1]; Landers earthquake in 1992 [2]; Northridge earthquake in 1994 [3]; Kobe earthquake in 1995 [4]; Marmara earthquakes in 1999 [5]; Chi-Chi earthquake in 1999 [6]; L'Aquila earthquake in 2009 [7]). The ground motions with directivity effect show larger spectral ordinates in medium to large period ranges. This larger spectral ordinates consequently impose larger demands on structures with periods close to pulse period [8, 9, 10, 11, 12, 13].

The directivity models proposed up to now try to catch the larger spectral ordinates and generally they can be classified into two groups known as broad-band and narrow-band models. Broad-band models amplify the response spectrum uniformly in medium to large period ranges while the narrow-band models amplify the response spectrum in narrow range of periods close to pulse period. Shahi and Baker [14] is an extended version of Tothong et al. [15] directivity model which modifies the seismic hazard framework in order to incorporate the effect of pulse period and pulse occurrence probability in seismic hazard analysis. Chiou and Spudich (2013) (hereafter CHS-13) is one of the most recent directivity

*Corresponding Author: saedmoghimi@aydin.edu.tr

Received: 03.04.2018 Accepted: 29.06.2018

models proposed in NGA west 2 directivity working group (Bayless and Somerville, Rowshandel, Shahi and Baker, Spudich and Chiou, and Chiou and Spudich – see [16]). These two directivity models are assembled in probabilistic seismic hazard analysis to derive amplification factors for the sites located around the faults. The significance of seismological and geometrical parameters on the level of spectral amplifications are investigated. The results are then used for development of simple amplification equations for incorporation of near fault effects in seismic design codes.

Both of the directivity models utilized in this study are categorized as narrow-band models. The model proposed by Shahi and Baker [14] (hereafter SHB-11) modifies the general framework of probabilistic seismic hazard analysis in order to account for the effect of probability of pulse occurrence and pulse period in spectral acceleration estimation. The Equation 1 shows the general framework of this model for calculation of annual exceedance rate:

$$v_{Sa}(x) = \sum_{i=1}^{\# \text{ faults}} v_i \iiint P^*(S_a > x | m, r, z, t_p) \cdot f_i(m, r, z) \cdot dm \cdot dr \cdot dz \cdot dt_p \quad (1)$$

where m , r , z and t_p represent magnitude, distance, source-to-site geometry and pulse period parameters respectively. In addition, $f_i(m, r, z)$ represents the probability density of occurrence of an earthquake scenario having magnitude m , distance r and fault-site geometry z , for fault i . The total probability of exceedance rate is calculated with considering the pulse occurrence and not occurrence probability in this equation. Equation 2 splits the probability of $S_a > x$ into two cases depending on whether or not the pulslike ground motion is observed: the first two probabilities on the right hand side are probabilities of observing a pulse and $S_a > x$ upon the occurrence of pulse. The last two probabilities consider observing no pulse and $S_a > x$ when no pulse is observed.

The model can estimate the response spectrum in any orientation with respect to fault strike. Since the pulse is mostly seen in fault normal direction for strike slip faults, the largest amplification occurs in this orientation in SHB-11 model. Therefore the response spectrum and consequently the amplification factor is calculated for fault normal component in this study. The geometrical parameters used in SHB-11 directivity model are shown in Figure 1.

$$P^*(S_a > x | m, r, z) = P(\text{pulse} | m, r, z) \cdot P(S_a > x | m, r, z, \text{pulse}) + [1 - P(\text{pulse} | m, r, z)] \cdot P(S_a > x | m, r, \text{no pulse}) \quad (2)$$

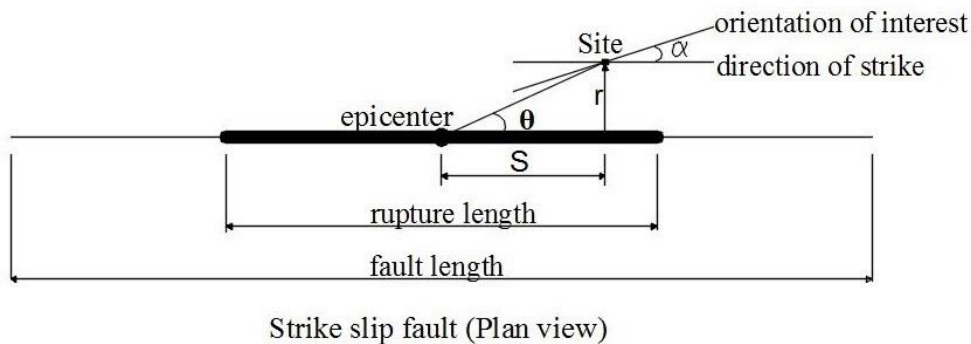


Figure 1. Source-to-site geometrical parameters used in SHB-11 for a strike-slip fault (r : closest distance between fault rupture and the site and S : distance to the site measured along the rupture). (Modified from Figure 4a in [14])

In CHS-13 directivity model, Direct Point Parameter is used to define directivity effect. The model is assembled on Chiou and Youngs [17] GMPE in order to predict RotD50 component (the component defined by [18] and used in NGA West2 GMPEs) with directivity effect. The Equation 3 shows the functional form of CHS-13 directivity model:

$$DPP = \ln(\hat{c}' \cdot \max(E, 0.1f) \cdot \max(\overline{FS}, 0.2)) \quad (3a)$$

$$\hat{c}' = \frac{1}{\left(\frac{1}{0.8} \frac{R_{HYP}-R_D}{E}\right)} \quad \text{for } E > 0 \quad (3b)$$

$$\hat{c}' = 0.8 \quad \text{for } E = 0 \quad (3c)$$

In this equation E is the distance between hypocenter (P_H) and direct point (P_D), f is the larger of fault length and width, \overline{FS} is the average S-wave radiation pattern over E-Path and \hat{c}' is the isochrone velocity. R_{HYP} ($\overline{P_H P_S}$), R_D ($\overline{P_D P_S}$) and E ($\overline{P_H P_D}$) are geometrical parameters that are shown in Figure 2. The direct point parameter is centered on average value of DPP for the sites with a constant distance from the fault rupture. This is because GMPEs take some directivity effect into account due to existence of impulsive ground motions in their dataset. The reader can refer to the relevant literature for more details about each model [14, 16].

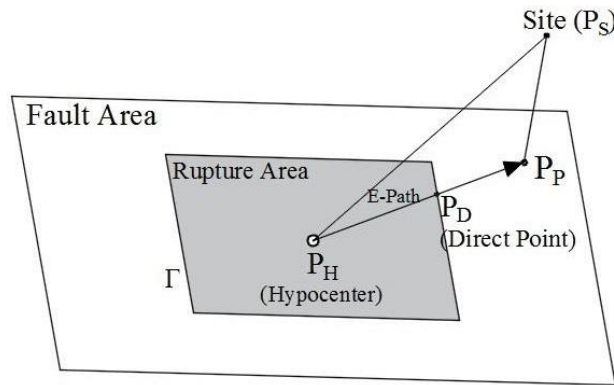


Figure 2. Illustration of Direct Point Parameter (DPP) from a fictitious source-site geometry: $\overline{P_H P_D}$ is the E-path with length E and P_D is the direct point

2. EVALUATION OF AMPLIFICATION FACTOR'S SENSITIVITY TO SEISMOLOGICAL AND GEOMETRICAL PARAMETERS

The first step in order to develop an amplification model for directivity effect is to investigate the effect of different seismological and geometrical parameters on the level of amplification. In this regard, Akkar et al. (2018) have implemented different earthquake scenarios on SHB-11 and CHS-13 directivity models to carry out a parametric study on the sensitivity of directivity amplification due to different geometrical and seismological parameters. The findings from Akkar et al. (2018) are utilized in this study in order to develop simplified amplification models, which are supposed to reflect the effect of directivity on design spectrum. In this section, the prominent findings from Akkar et al. (2018) which are used in the development of directivity amplification models are discussed and explained briefly. The reader is referred to Akkar et al. (2018) for more details.

In order to study the effect of different seismological and geometrical parameters on the level of amplification probabilistic hazard analysis have been done for 42 sites spatially distributed around the fault (

Figure 3) with and without considering directivity effect. The response spectrum is calculated for each case and the amplification is then calculated from the normalization of response spectrum with directivity effect ($S_{a_{directivity}}$) to conventional response spectrum ($S_{a_{normal}}$). The amplification factor is calculated for two hazard levels (475-year and 2475-year return periods). Different fault lengths are considered in the hazard analysis (FL=20, 50, 100, 150 and 300km) with constant width for all cases (Fault Width=10km). Three seismicity levels (low, medium and high) are considered for each case with slip rate values equal to SR=0.5, 1.0 and 2.0cm/year respectively.

Figure 4 shows the spatial distribution of amplification for both SHB-11 and CHS-13 models at spectral period 4.0sec for the fault with 100km length, SR=2.0cm/year and 475-year return period. As can be seen from this figure, the sites located along the $R_x/L = 0.5$ line and R_y less than 10km experience the highest amplification in SHB-11 model. This is because of the pulse occurrence probability distribution pattern in SHB-11 model which shows larger values for the sites located near the edge of the fault. In CHS-13 the maximum amplification occur for the sites located beyond the fault edges. This is due to the direct point distribution pattern in CHS-13 model which reach the maximum values in the sites along $R_x/L=0.6$.

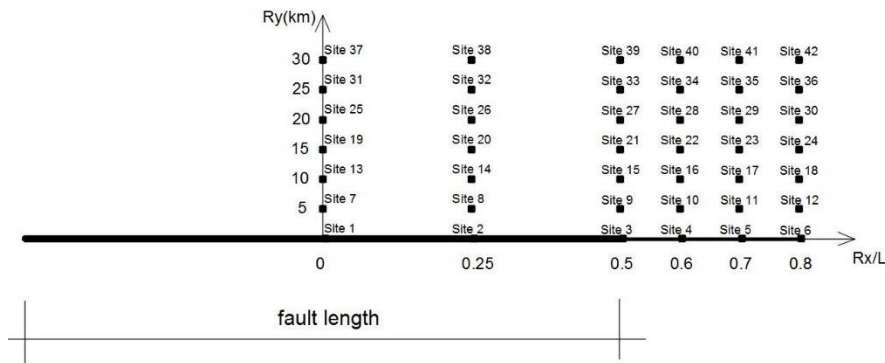


Figure 3. Spatial distribution of the sites around the fault

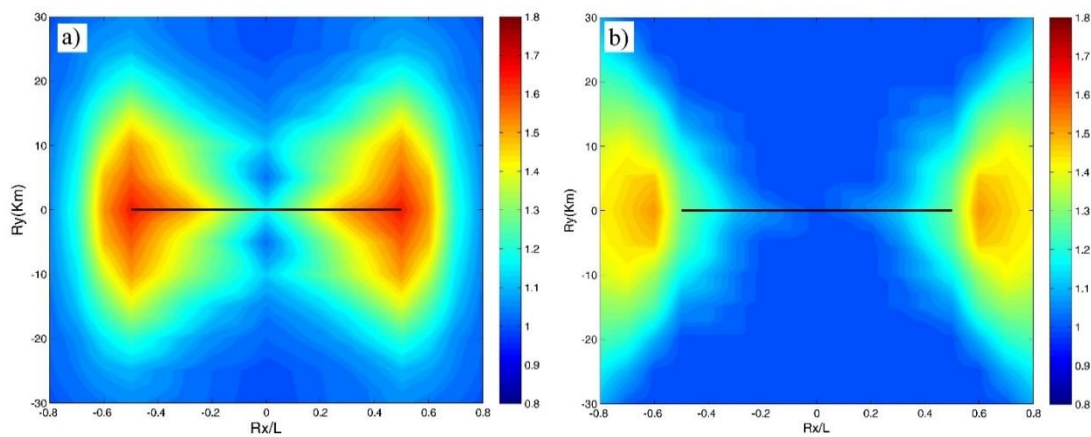


Figure 4. Amplification factor contour map for 100km length fault, Slip rate=2cm/year and 475 year return period spectrum, T=4sec. a) Shahi and Baker 2011, b) Chiou Spudich 2013

Figure 5 shows the amplification factor for two faults with different lengths (and hence two different characteristic magnitudes) for both SHB-11 and CHS-13 models. The amplification is plotted for 42 sites together with their median value. Several features can be seen in this figure. Both SHB-11 and CHS-13 models have a bilinear trend for the amplification factor. The difference between these two models is that SHB-11 model tends to amplify the response spectrum in a narrow range of period while CHS-13 model amplifies the spectrum in a wider range of periods. This is due to the fact that SHB-11 model tries to amplify the S_a at periods close to the period of the directivity pulse (T_p). In addition, SHB-11 shows larger amplification values because as stated before this model estimates fault normal component which is more likely to have impulsive waveforms and consequently larger spectral accelerations. The amplification factor in SHB-11 reaches the maximum value at a spectral period (T_{max}) followed by a descending trend for larger periods. The amplification factor in CHS-13 has an ascending trend up to spectral period called as T_{corner} . For the periods greater than T_{corner} the amplification has plateau form and is almost constant.

The spectral period that maximum amplification occur in both SHB-11 and CHS-13 models depend on characteristic magnitude of the fault, meaning that the larger is the characteristic magnitude, the greater is the spectral period that maximum amplification occur. Fault magnitude can also affect on the amplitude of amplification. As can be seen from Figure 5, the amplitude of amplification increases with fault magnitude increment for both SHB-11 and CHS-13 models. Therefore, the fault magnitude not only affects on the level of amplification but also changes the period that maximum amplification occur. Akkar et al. [19] show that fault magnitude and the maximum amplification factor ($Mw-AMP(T_{max})$) have a linear relationship.

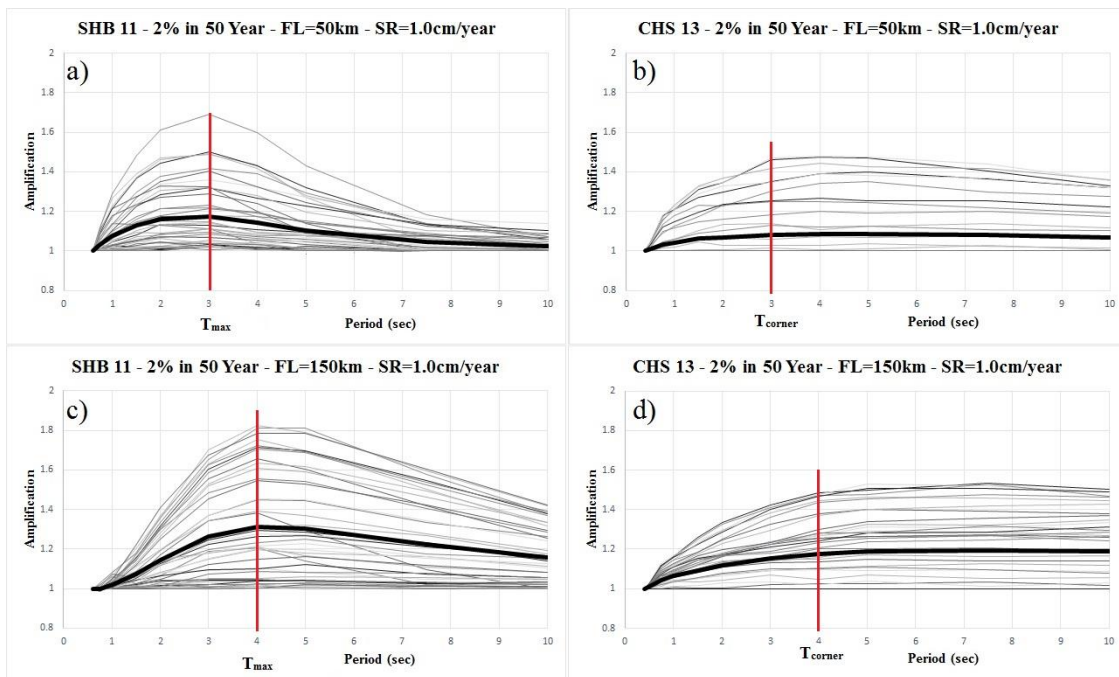


Figure 5. 2475-year amplification factor plots for 42 sites spatially distributed around the fault and related median curves a) SHB11 - 50km fault length, b) CHS13 - 50km fault length, c) SHB11 – 100km fault length d) CHS13 - 100km fault length

Akkar et al. [19] also show that slip rate and hazard level are determining parameters on the level of amplification in SHB-11 model. They indicate that the median of amplification for 42 sites shows 11.5% increment at spectral period $T=4$ sec for the fault with 100km length and 475-year return period when the slip rate increases from 0.5 to 2.0cm/year. Akkar et al. [19] also show that the amplification factor

has larger values for greater return periods. In CHS-13 model it is shown that the slip rate and hazard level do not affect on the level of amplification considerably.

3. AMPLIFICATION MODELS

As discussed in previous section the amplification curves have a bilinear trend in both SHB-11 and CHS-13 models. In both models the amplification has an increasing trend starting from 1 and reaching the maximum value at spectral period T_{max} in SHB-11 and T_{corner} in CHS-13 models. While the amplification has descending trend for periods larger than T_{max} in SHB-11, it takes almost constant value for the periods greater than T_{corner} in CHS-13 (Figure 5). It is shown that the period that the amplification reaches the maximum value has a linear relationship with characteristic magnitude of the fault [19]. This relationship is shown in Equation 4.

$$T_{mc} = 2.7233 \times M_w - 15.373 \quad (4)$$

where T_{mc} denotes to T_{max} in SHB-11 and T_{corner} in CHS-13 models and M_w is the characteristic magnitude of the fault.

In SHB-11 model the amplification equation is extracted for the sites located along $R_x/L=0.5$ and R_y less than 15km (Sites 3, 9, 15 and 21 in

Figure 3). For this purpose the median of amplification is calculated at T_{max} and $T=10$ sec for these sites. The amplification is equal to 1.0 at $T=0.6$ sec for all cases. For the other spectral periods the amplification is calculated form linear interpolation as can be seen from Equation 5.

$$AMP = 1 + [(AMP_{(T_{max})} - 1) \times (\frac{T-0.6}{T_{max}-0.6})] \quad 0.6\text{sec} < T < T_{max} \quad (5a)$$

$$AMP = AMP_{(T_{max})} + [(AMP_{(T=10)} - AMP_{(T_{max})}) \times (\frac{T-T_{max}}{10-T_{max}})] \quad T_{max} < T < 10\text{sec} \quad (5b)$$

As stated in the last section the amplification at T_{max} and $T=10$ sec has a linear relationship with characteristic magnitude. The maximum amplification and the amplification at $T=10$ sec are calculated from Equation 6:

$$AMP(T_{max}) = \alpha_{T_{max}} \times M_{ch} + \beta_{T_{max}} \quad 6.25 < M_{ch} \leq 7.25 \quad (6a)$$

$$AMP(T_{max}) = \alpha_{T_{max}} \times 7.25 + \beta_{T_{max}} \quad M_{ch} > 7.25 \quad (6b)$$

$$AMP(T = 10) = \alpha_{T10} \times M_{ch} + \beta_{T10} \quad M_{ch} > 6.25 \quad (6c)$$

in which M_{ch} is the mean moment magnitude, M_w , that is estimated from the empirical M_w vs. RA relationship of Wells and Coppersmith [20]. The related coefficients which are extracted from the fitted functions are illustrated in Table 1 and Table 2 for $AMP_{(T_{max})}$ and $AMP_{(T=10\text{sec})}$ respectively.

Table 1. $\alpha_{T_{max}}$ and $\beta_{T_{max}}$ coefficients for $AMP(T_{max})$ – SHB-11

AMP(T_{max}) SR(cm/year)	475-year Return Period		2475-year return period	
	$\alpha_{T_{max}}$	$\beta_{T_{max}}$	$\alpha_{T_{max}}$	$\beta_{T_{max}}$
SR=0.5	0.146	0.149	0.495	-1.9
SR=1.0	0.241	-0.364	0.546	-2.168
SR=2.0	0.454	-1.664	0.554	-2.167

Table 2. α_{T10} and β_{T10} coefficients for AMP(T=10sec) – SHB-11

AMP(T10) SR(cm/year)	475-year Return Period		2475-year return period	
	α_{T10}	β_{T10}	α_{T10}	β_{T10}
SR=0.5	0.045	0.72	0.313	-0.95
SR=1.0	0.167	-0.04	0.384	-1.4
SR=2.0	0.229	-0.4	0.425	-1.65

The amplification equation that is proposed for CHS-13 model has a similar layout to the amplification equation proposed for SHB-11 in previous section with only two differences. As stated before, the amplification model for CHS-13 has an increasing part from T=0.5sec to the spectral period T_{corner} followed by a plateau form for period range $T_{corner} < T < 10$ sec. The amplification equation is extracted by taking the median of amplification for the sites located along $R_x/L=0.6$ and R_y less than 15km (Sites 4, 10, 16 and 22 in

Figure 3). The amplification model for CHS-13 is shown in Equation 7. $AMP(T_{corner})$ is also calculated from Equation 8:

$$AMP(T) = 1 + \left[(AMP(T_{corner}) - 1) \times \frac{T-0.5}{T_{corner}-0.5} \right] \quad 0.5 < T \leq T_{corner} \quad (7a)$$

$$AMP(T) = AMP(T_{corner}) \quad T_{corner} < T < 10 \quad (7b)$$

$$AMP(T_{corner}) = (\alpha_{T_{corner}} \times M_{ch} + \beta_{corner}) \quad 6.25 < M_{ch} \leq 7.25 \quad (8a)$$

$$AMP(T_{corner}) = (\alpha_{T_{corner}} \times 7.25 + \beta_{T_{corner}}) \quad M_{ch} > 7.25 \quad (8b)$$

The coefficients for linear fitted equation of $AMP(T_{corner})$ are provided in Table 3.

Table 3. α and β coefficients for linearly fitted $AMP(T_{corner})$ function - CHS-13

475-Year		2475-Year	
$\alpha_{T_{corner}}$	$\beta_{T_{corner}}$	$\alpha_{T_{corner}}$	$\beta_{T_{corner}}$
0.4	-1.4931	0.464	-1.9

As stated before the amplification equations for SHB-11 and CHS-13 models are extracted from the sites within 15km which have the largest amplification values. The amplification effect is attenuated for the sites with larger distances and it is totally disappeared for the sites located in 30km distance from the fault. A distance taper function is applied to the amplification models in order to consider the effect of this attenuation. The distance taper function is shown in Equation 9.

$$AF = AMP \quad R_{jb} \leq 10 \text{km} \quad (9a)$$

$$AF = AMP + \left[(1 - AMP) \times \left(\frac{R_{jb} - 10}{20} \right) \right] \quad 10 \text{km} < R_{jb} \leq 30 \text{km} \quad (9b)$$

$$AF = 1 \quad R_{jb} > 30 \text{km} \quad (9c)$$

where the AMP denotes to the amplification factor calculated from equations of both SHB-11 and CHS-13 models proposed in the this section.

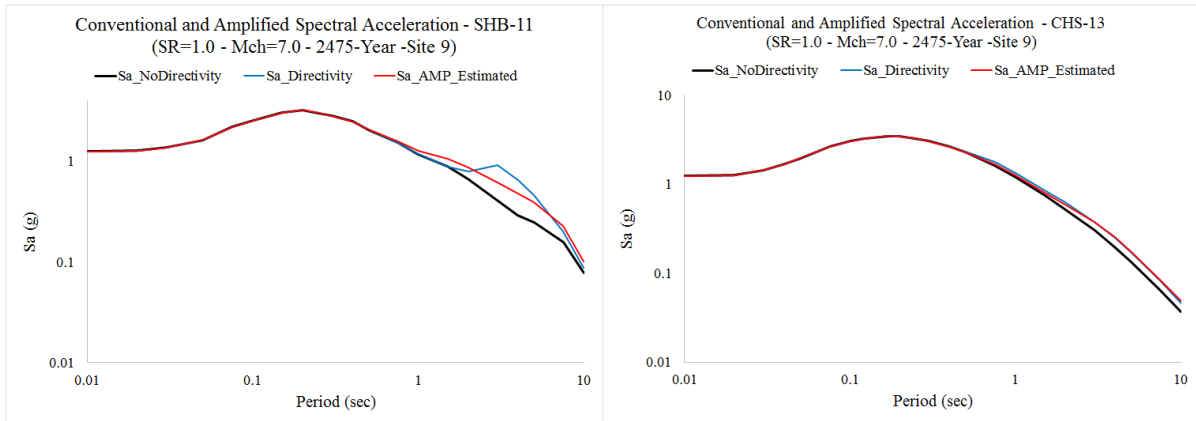


Figure 6. Conventional and Amplified Spectral Acceleration

The amplification model proposed in this section is used to calculate the amplified spectral acceleration coordinates for a site located 5km away from the edge of the fault with 100km length ($M_{ch}=7.0$). Figure 6 illustrates and compares 2475-year spectral acceleration calculated from conventional and directivity included PSHA together with spectral acceleration calculated from the amplification models f for both of SHB-11 and CHS-13. As discussed in Section 2 the sites located near the fault edge are exposed to largest directivity amplification and the amplification models proposed here have good estimates for the amplified spectral accelerations of these sites as can be seen in Figure 6.

4. CONCLUSION

The results of hazard analysis show that the amplification reaches the maximum values for the sites located near the edge of fault for both SHB-11 and CHS-13 models. The period that maximum amplification occur is the same for both models and it has a linear relationship with characteristic magnitude of the fault. SHB-11 amplifies the response spectrum in a narrower range of periods compared with CHS-13. SHB-11 shows larger amplification values compared with CHS-13 which is because of component that these models estimate. While CHS-13 estimates $RotD50_{Directivity}$, SHB-11 predicts fault normal component which usually shows larger spectral ordinates due to existence of impulsive waveforms. The results of analysis show that slip rate, characteristic magnitude of the fault and hazard level are all important parameters in determination of amplification level in SHB-11 model. In CHS-13 model slip rate and hazard level do not affect on the level of amplification considerably but the characteristic magnitude of the fault is still important. In the last part of this study, we implemented simple and applicable rules on the hazard results to propose amplification equations for the directivity effect. These relationships can be considered in design codes for incorporation of near fault effects.

REFERENCES

- [1] Housner GW and Hudson DE “The Port Hueneme earthquake of March 18, 1957,” Bull. Seismol. Soc. Am., vol. 48, no. 2, pp. 163–168, 1958.
- [2] Campbell K and Bozorgnia Y. “Empirical analysis of strong ground motion from the 1992 Landers, California, earthquake,” Bull. Seismol. Soc. Am., vol. 84, no. 3, p. 573, 1994.
- [3] Somerville P, Saikia C, Wald D and Graves R “Implications of the Northridge earthquake for strong ground motions from thrust faults,” Bull. Seismol. Soc. Am. , vol. 86, no. 1B, pp. S115–S125, Feb. 1996.

- [4] Fukushima Y, Irikura K, Uetake T and Matsumoto H, “Characteristics of observed peak amplitude for strong ground motion from the 1995 Hyogoken Nanbu (Kobe) earthquake,” *Bull. Seismol. Soc. Am.*, vol. 90, no. 3, pp. 545–565, 2000.
- [5] Akkar S and Gulkan P, “Near-field earthquakes and their implications on seismic design codes,” Rep. No. METU/EERC 01-01, Earthq. Eng. Res. Center, Middle East Tech. Univ. Ankara, Turkey, 2001.
- [6] Chen KC, Huang BS, Wang JH, Huang WG, Chang TM, Hwang RD, Chiu HC and Tsai C-C P, “An Observation of Rupture Pulses of the 20 September 1999 Chi-Chi, Taiwan, Earthquake from Near-Field Seismograms,” *Bull. Seismol. Soc. Am.*, vol. 91, no. 5, pp. 1247–1254, Oct. 2001.
- [7] Chioccarelli E and Iervolino I, “Near-source seismic demand and pulse-like records: A discussion for L’Aquila earthquake,” *Earthq. Eng. Struct. Dyn.*, vol. 39, no. 9, pp. 1039–1062, 2010.
- [8] Alavi B and Krawinkler H, “Behavior of moment-resisting frame structures subjected to near-fault ground motions,” *Earthq. Eng. Struct. Dyn.*, vol. 33, no. 6, pp. 687–706, 2004.
- [9] Sasani M and Bertero VV, “Importance of Severe Pulse-Type Ground Motions in Performance-Based Engineering: Historical and Critical,” in *Proceedings of the 12th World Conference on Earthquake Engineering*, New Zealand Society for Earthquake Engineering, Upper Hutt, New Zealand, 2000.
- [10] Akkar SD, Yazgan U and Gülkan P, “Deformation Limits for simple Non-Degrading Systems subjected to Near-Fault Ground Motions,” in *Proceedings 13th World Conference on Earthquake Engineering*, 2004, no. 2276, pp. 1–14.
- [11] Gillie JL, Rodriguez-Marek A and McDaniel C, “Strength reduction factors for near-fault forward-directivity ground motions,” *Eng. Struct.*, vol. 32, no. 1, pp. 273–285, 2010.
- [12] Ruiz-García J, “Inelastic Displacement Ratios for Seismic Assessment of Structures Subjected to Forward-Directivity Near-Fault Ground Motions,” *J. Earthq. Eng.*, vol. 15, no. 3, pp. 449–468, 2011.
- [13] Sehhati R, Rodriguez-Marek A, ElGawady M and Cofer WF, “Effects of near-fault ground motions and equivalent pulses on multi-story structures,” *Eng. Struct.*, vol. 33, no. 3, pp. 767–779, 2011.
- [14] Shahi SK and Baker JW, “An empirically calibrated framework for including the effects of near-fault directivity in probabilistic seismic hazard analysis,” *Bull. Seismol. Soc. Am.*, vol. 101, no. 2, pp. 742–755, 2011.
- [15] Tothong P, Cornell CA and Baker JW, “Explicit directivity-pulse inclusion in probabilistic seismic hazard analysis,” *Earthq. Spectra*, vol. 23, no. 4, pp. 867–891, 2007.
- [16] Spudich P, Bayless J, Baker J, Chiou BSJ, Rowshandel B, Shahi S and Somerville P, “Final Report of the NGA-West2 Directivity Working Group,” 2013.
- [17] Chiou BSJ and Youngs RR, “Update of the Chiou and Youngs NGA model for the average horizontal component of peak ground motion and response spectra,” *Earthq. Spectra*, vol. 30, no. 3, pp. 1117–1153, 2014.

- [18] Boore DM, “Orientation-Independent, Nongeometric-Mean Measures of Seismic Intensity from Two Horizontal Components of Motion,” *Bull. Seismol. Soc. Am.*, vol. 100, no. 4, pp. 1830–1835, 2010.
- [19] Akkar S, Moghimi S and Arıcı Y, “A study on major seismological and fault-site parameters affecting near-fault directivity ground-motion demands for strike-slip faulting for their possible inclusion in seismic design codes,” *Soil Dyn. Earthq. Eng.*, vol. 104, no. January 2018, pp. 88–105, 2018.
- [20] Wells DL and Coppersmith KJ, “New Empirical Relationships among Magnitude, Rupture Length, Rupture Width, Rupture Area, and Surface Displacement,” *Bull. Seismol. Soc. Am.*, vol. 84, no. 4, pp. 974–1002, 1994.